bioRxiv preprint doi: https://doi.org/10.1101/2022.07.22.501162; this version posted July 24, 2022. The copyright holder for this preprint (which was not certified by peer review) is the author/funder, who has granted bioRxiv a license to display the preprint in perpetuity. It is made available under aCC-BY-ND 4.0 International license.

Event-based vision sensor enables fast and dense single-molecule localization microscopy

Clément Cabriel[1,*], Christian G. Specht[2], and Ignacio Izeddin[1,**]

[1]Institut Langevin, ESPCI Paris, Université PSL, CNRS, 75005 Paris, France
[2]DHNS, Inserm U1195, Université Paris-Saclay, 94276 Le Kremlin-Bicêtre, France
[*]Corresponding author: clement.cabriel@espci.fr, cabriel.clement@gmail.com
[**]Corresponding author: ignacio.izeddin@espci.fr

July 22, 2022

Single-molecule localization microscopy (SMLM) applications are often hampered by the fixed frame rate at which data acquisition is performed. Here, we present an alternative new approach of acquiring and processing SMLM data based on an event-based (or neuromorphic vision) sensor. This type of sensor reacts to light intensity changes rather than integrating the number of photons during each frame exposure time. This makes them particularly suited to SMLM, where the ability to surpass the diffraction-limited resolution is provided by blinking events. Each pixel works independently and returns a signal only when an intensity change is detected; intensity changes are returned as a list with pixel positions and timestamps rather than frames with a fixed frame rate. Since the output is a sparse list containing only useful data (for example a molecule turning on or off), the temporal resolution is significantly faster than typical speeds of EMCCD and sCMOS cameras. Here we demonstrate the feasibility of SMLM super-resolution imaging with this type of event-based sensors which, in addition, are more affordable than EMCCD or sCMOS cameras. We characterize the localization precision and show that it is equivalent to that of frame-based scientific cameras, including on fluorescently labelled biological samples. Furthermore, taking advantage of the unique properties of the sensor, we use event-based SMLM to perform very dense single-molecule acquisitions, where frame-based cameras experience significant limitations. All the data processing codes are made available.

Introduction

The advent of single-molecule localization microscopy (SMLM) fifteen years ago brought an improvement in image resolution in fluorescence microscopy by a factor of 10 [1, 2, 3] and has become an invaluable tool for cell biology as it can resolve cellular structures with nanometer resolution. Since then, significant advancements have been possible through the development of new optical techniques, e.g. achieving sub-nanometric localization [4, 5], ingenious labeling methods [6, 7, 8] or the synthesis of brighter dyes compatible with live-cell imaging [9, 10], not to mention numerous application-specific or more general data treatment methods [11, 12, 13]. These advances address some of the remaining challenges in SMLM, including but not limited to imaging thick samples and tissues, reducing phototoxicity and photobleaching for live-cell imaging, but also obtaining quantitative information on the distribution, size, shape, spatial organisation and stoichiometry of macromolecular complexes in order to steer biological interpretation. For a recent review of the field of SMLM, refer to [14, 15]

While retrieving the positions of single molecules is pivotal in applications as varied as 3D imaging of immunolabelled samples [16, 17, 18, 19], spatial analysis of protein clusters [20, 21] or protein

bioRxiv preprint doi: https://doi.org/10.1101/2022.07.22.501162; this version posted July 24, 2022. The copyright holder for this preprint (which was not certified by peer review) is the author/funder, who has granted bioRxiv a license to display the preprint in perpetuity. It is made available under aCC-BY-ND 4.0 International license.

dynamics in the cell [22], single-molecule microscopy is also used in a much broader range of applications exploiting other information carried by the point-spread function (PSF). A non exhaustive list of them includes accessing the spectrum of the dyes for multicolor imaging [23, 24], retrieving the emitter's orientation via polarization measurements [25], or even probing the local environment of the molecules through modifications of the fluorescence intensity [26, 27], or the fluorescent state lifetime [28, 29, 30, 31].

Regardless of their use, single-molecule experiments are routinely limited by the acquisition speed to a certain extent. On the one hand, SMLM experiments routinely require more than 20000 frames, which represents tens of minutes of acquisition with exposure times in the 10 ms–50 ms range. On the other hand, the chosen exposure time sets a hard limit on the temporal scale at which fast dynamic processes are observable. While the importance of temporal resolution is obvious in live cells, where it determines the range of dynamic processes that can be studied, it cannot be overlooked in experiments with fixed samples—(d)STORM buffers suffer from oxidation with time, long experiments require proper 3D stability of the sample etc. More generally, improving the acquisition rate allows more efficient data collection, which can be important to better describe biological phenomena and improve statistical significance. In some cases, it can even be used to develop automated high throughput data collection setups and analysis workflows [32, 33].

Improving the data recording rate, however, is no small task, as frame-based scientific cameras (EMCCD and sCMOS) work at a fixed frame rate chosen before the acquisition. Even assuming that the camera is able to work at the desired speed without any significant dead time between frames or unreasonable cropping of the camera chip, this imposes a compromise between the temporal bandwidth and the quality of the signal (shorter exposure leads to higher relative noise). Besides, it also raises serious issues whenever the spatial distribution of proteins in the sample is heterogeneous, or when different targets in the experiment obey dynamic processes at different time scales. This can be the case in Single Particle Tracking (SPT) studies if the protein of interest undergoes large variations of diffusivity in time and/or space over the course of the acquisition, or in the case of structural imaging of fixed samples, when the use of an excitation with a Gaussian profile causes the center and the edges of the region of interest to blink at different rates. In any case, the frame rate typically has to be adapted to the fastest processes or the highest densities, which leads to a detrimental increase of noise.

On the other hand, event-based sensors (also sometimes called neuromorphic or dynamic vision sensors) use a very different principle than frame-based cameras. An event-based sensor is an array of pixels that each function independently of the others, and are sensitive to intensity changes rather than to an average irradiance over a fixed exposure time. Although each pixel has a response time (in the range of a few µs to a few hundreds of µs), it does not work at a fixed frame rate. Instead, it returns a signal called 'event' after it detects a change of irradiance. Therefore, only meaningful data is recorded (as long as a pixel does not detect a change, it does not return any output signal), which potentially allows a vast increase of data collection rate compared to scientific cameras, as the maximum data transfer rate is almost never a limiting factor in event-based sensors. As a comparison, the fraction of camera-recorded data effectively used for localization purposes varies from around 5 to 10 % in the case of a (direct) Stochastic Optical Reconstruction Microscopy ((d)STORM) experiment with very dense Point Spread Functions (PSFs) in each frame, to less than 0.1 % in sparse SPT experiments, taking into account that the localization program calculates the position from a small Region Of Interest (ROI) around the center of the PSF and discards the rest of the data. Event-based sensors are relatively new on the market but typically target industrial applications rather than bioimaging. They typically have pixel numbers of the order of a million, and a pixel size of the order of 10 µm, making them quite straightforward to include in a typical fluorescence microscopy setup. Finally they are generally more affordable than sCMOS and EMCCD cameras.

Here, we propose an implementation of single-molecule localization experiments with an event-

bioRxiv preprint doi: https://doi.org/10.1101/2022.07.22.501162; this version posted July 24, 2022. The copyright holder for this preprint (which was not certified by peer review) is the author/funder, who has granted bioRxiv a license to display the preprint in perpetuity. It is made available under aCC-BY-ND 4.0 International license.

based sensor, which, to the best of our knowledge, has never been reported before. Incidentally, we are not aware of any reported use of event-based sensors in fluorescence microscopy or in cell biology. We will describe the principle of event-based sensing in more detail and the data processing steps. We then characterize the response of the sensor to a fluorescent signal and assess the localization precision. We furthermore demonstrate the detection of organic dyes for single-molecule fluorescence imaging and use it to produce a super-resolution image of a fixed immunolabelled sample. Finally, we use the unique features of event-based sensing to improve localization performance in the case where the density of molecules is high and PSF overlaps cause frame-based algorithms to fail.

Principle, optical setup and data display

An event-based sensors is a rectangular or square array of pixels that are sensitive to optical intensity variations only. For a technological review about event-based sensing, readers may refer to [34]. Since each pixel works independently of the rest of the array, the principle of the sensor can be described through the response of one pixel. At each time t, the light intensity $I(t)$ (i.e. number of photons incoming on the pixel per unit time) is linearly converted into an electronic response. The pixel stores a reference level $I_{\text{ref}}(t)$, which is then used to detect meaningful variations of the intensity relative to this reference level. Two thresholds B_+ and B_- are used to set the sensitivity and can be modified. They are used respectively to detect an increase and decrease in intensity. While B_+ and B_- can be set to different values (all pixels use the same values of B_+ and B_-, which are set as input parameters but can be modified during the acquisition if required), we always use equal values (called B) in this work and therefore symmetric positive and negative detections. According to the specifications given by the manufacturer, the intensity variation detection is logarithmic rather than linear. Therefore, a signal is triggered as soon as $\log(I(t)/I_{\text{ref}}(t)) > B_+$ (positive event) or $\log(I(t)/I_{\text{ref}}(t)) < B_-$ (negative event). The principle of the response of a pixel is illustrated in **Fig. 1a**, and we show in **Fig. 1b** how varying the values of the sensitivity B changes the output signal. From a quantitative point of view, these thresholds can be as low as 30 % of the reference level. Whenever an event is triggered, the sensor returns a signal containing the x and y pixel coordinates, the polarity (positive or negative) and the time of the trigger. These coordinates are added to the output file. After the event is triggered, the value of the reference level is replaced with the value of the intensity at the time of the trigger. As a consequence, a large variation of the signal will cause the pixel to return several events in a quick succession, which readily provides a certain *quantitativity* in the detection.

When compared to scientific cameras (whether EMCCD or sCMOS), the event-based sensor behaves differently on several points. First, it detects only intensity changes (in our case, a molecule turning on or off, or the motion of a moving emitter). As long as the intensity stays close to the reference level within the tolerance threshold, the pixel does not respond. This offers very promising perspectives when it comes to implementing live data processing and image reconstruction, or even high-throughput automated experiments, where the volume of data is sometimes so high that the raw data has to be discarded. Another difference between scientific cameras and event-based sensors is the dynamic range, which is vastly superior for the event-based sensor, making it almost impossible to saturate the sensor with fluorescence signals, which can become problematic when using bright fiducial markers. In other words, large contrasts (which can be limiting especially in the case of EMCCD cameras where saturation can occur for moderate signals) are rarely a problem with event-based sensors. However, the most significant difference between the two types of detectors is probably the fact that the event-based sensor does not use a fixed frame rate and thus does not return a limited number of frames. This implies that the temporal resolution of the acquisition is not limited by user-defined parameters. While the temporal bandwidth is not infinite (each pixel has a certain response time in the range of a few µs to a few hundreds of µs [35]), the time resolution is usually determined in the processing stage by the time base used for the data treatment. This feature is very interesting for SMLM imaging since it allows to process the same dataset with different time bases to investigate biological processes at different time scales. The differences between the responses of a scientific camera and an event-based sensor are summarized in **Fig. 1c**. A further difference is the

bioRxiv preprint doi: https://doi.org/10.1101/2022.07.22.501162; this version posted July 24, 2022. The copyright holder for this preprint (which was not certified by peer review) is the author/funder, who has granted bioRxiv a license to display the preprint in perpetuity. It is made available under aCC-BY-ND 4.0 International license.

quantitativity of the signal: scientific cameras are more adapted for quantitative intensity measurements provided the exposure time is properly matched to the biological or photochemical processes of interest. Nevertheless, as we will further investigate in this paper, the event-based sensor still provides some quantitative information which lies in the number of events generated by an intensity transition—a dim or a bright molecule produce different numbers of events when they turn on or off. This is further controllable by tuning the sensitivity threshold B, as illustrated in **Fig. 1b**.

We used such an event-based sensor in an optical setup designed for SMLM experiments presented in **Fig. 1d**. It is essentially a standard wide-field microscope with a high numerical aperture collection. The detection path is built to offer some modularity by distributing the fluorescence light in either one or both of the sensors, the EMCCD and the event-based sensor—this will be useful later in the characterization and comparison of their relative performance. With regards to data display and processing, several approaches are conceptually possible, and we propose two complementary displays. A purely frame-based approach is proposed in **Fig. 1e**. Frames are generated by binning all the events in a certain time interval Δt in a pixelized canvas, respecting also the sign of events (each positive event is counted as +1 and each negative as -1). This visualization method emphasizes the spatial distribution of events at the expense of some time resolution. In **Fig. 1e**, we represent data acquired on 200 nm fluorescent beads deposited on a coverslip and excited with a square pulsed excitation with a duty cycle of 50 % at 10 Hz and a frame reconstruction at Δt = 10 ms. The rising and falling edges of $I(t)$ are clearly visible, as well as the near absence of output signal when the intensity is constant, whether the source is emitting or not. Note the sharp signal at frames 10 ms–20 ms and 60 ms–70 ms, when the excitation turns on and off respectively. On the contrary, no signal is returned between 30 ms and 60 ms, when the bead is emitting light with a constant power. Finally, one can note on frames 20 ms–30 ms and 70 ms–80 ms that the signal is not returned instantly—more specifically, the dimmer pixels at the edge of the PSF respond more slowly which explains the visible rings (we attribute this to the time necessary to sample the photons into an intensity measurement). **Fig. 1e** furthermore highlights the quantitative aspect of the detection—the bead at the bottom left is less bright and thus generates fewer events. This frame-based display has the advantages of clarity, as it is very similar to the familiar frames acquired by scientific cameras, and spatial information conservation (the PSFs can be seen to be spread on several pixels like on camera frames). Although the time bin can easily be varied in post-processing to change the time scale, we find that for certain applications, it is poorly suited to accurately investigate the time response of the imaging system and/or of the biological sample studied. From a conceptual point of view, representing essentially sparse data with a dense matrix is also somewhat unadapted. Therefore, we propose in **Fig. 1f** an complementary data display based on temporal profiles (i.e. time traces of the number of detected events) over all the pixels of a PSF, which we find adequately highlights the nature of the signal returned by the event-based sensor. Although this representation also relies on time binning, it is typically done with much lower values of Δt, which is more suited for the study of the time response of single molecules. This comes at the cost of a certain loss of spatial information, as all the pixels in a PSF are summed together. **Fig. 1f** incidentally reveals two unexpected features—first, there is a slight imbalance between the numbers of total positive and negative events in one cycle, and second the negative events seem on average slower than the positive events. We do not have an explanation for this effect, but we assume it can easily be addressed by tuning the electronics coupled to the event-based sensor. For the sake of simplicity and easy implementation for this work, we decided to use the sensor out-of-the box, without further modifications.

Although the temporal bandwidth is not defined by the acquisition parameters, the processing algorithms have to be carefully designed to account for the time scales that match the desired biological application. We highlight this in **Fig. 1g** by displaying the signal returned by 40 nm fluorescent beads deposited on a coverslip illuminated with a continuous excitation during the translation of the sample using the piezo stage. A small time bin (Δt = 1 ms) efficiently samples the dynamic to reveal two opposed lobes—a positive leading edge and a negative trailing edge. This comes at the cost of a relatively modest number of events. On the contrary, increasing the time bin to Δt = 10 ms

bioRxiv preprint doi: https://doi.org/10.1101/2022.07.22.501162; this version posted July 24, 2022. The copyright holder for this preprint (which was not certified by peer review) is the author/funder, who has granted bioRxiv a license to display the preprint in perpetuity. It is made available under aCC-BY-ND 4.0 International license.

provides a large number of events for a better statistical set, which is spoiled by a dramatic motion blur as well as a loss of resolution. Obviously, the value of the time bin has to be matched to the phenomenon under investigation, but no knowledge or assumption is required prior to the acquisition (contrary to scientific camera-based approaches), as the selection of Δt is done as part of the processing workflow. This could even be used to perform a multi-timescale processing (either using a single multiscale workflow or running several single-scale algorithms with different time bases) on the same dataset to extract both slow and fast processes. It is interesting to notice that the use of an event-based sensor readily provides an efficient way to manage the molecule density by performing a spatio-temporal resampling, as we will highlight more in detail in the section **Event-based high density imaging**.

Single molecule localization

We then set out to use the event-based detection microscope to detect and localize single molecules, focusing on blinking fluorophores such as in (d)STORM or PALM microscopy. Our processing approach to single-molecule localization is partly frame-based. Events from the raw output list are binned into frames with a given Δt (typically between 10 ms and 50 ms), which are used for PSF detection. This step is done on the positive events only (i.e. when the molecule turns on) using a wavelet decomposition algorithm described in [11]. Then, each molecule is localized using a subset of events corresponding to a spatial ROI of ± 4 pixels (i.e. a total area of 9x9 pixels = 600 nm) around the center of the PSF, and a temporal ROI of $[T_0 - \delta T_{\text{start}}, T_0 + \delta T_{\text{end}}]$ around the timestamp of the frame T_0, with the (negative) lower boundary δT_{start} around 20 ms to 60 ms, and the upper boundary δT_{end} around 80 ms to 200 ms (δT_{end} has to be sufficient to cover the full ON time of the molecule). In this subset of events, the x and y positions are determined by calculating the center of mass of all the events. Moreover, complementary information can also be extracted, such as the number of positive and negative events N_+ and N_-, the time when the molecule turns on t_+ (taken as the mean of the times of the positive events) and the time when it turns off (mean of the times of the negative events) and the ON time, defined as $t_{ON} = t_- - t_+$. Finally, the drift is corrected using a direct cross correlation algorithm (in other words, the reference is the sample image itself rather than fiducial markers).

As a first step, we aimed at assessing the localization precision. To this end, we used a regime where both a classical scientific camera and an event-based sensor return a signal that can be used for localization precision measurement. We deposited fluorescent beads on a coverslip in PBS, and we illuminated them with a square-modulated laser at 10 Hz. A 30:70 (EMCCD:event-based sensor) beamsplitter was used in the detection path. The exposure time of the EMCCD was set to 100 ms (i.e. one period exactly), thus yielding a constant signal on which the localization precision could be measured from many frames. The sensitivity of the event-based sensor was set to different arbitrary values, and the output signal was binned in 100 ms frames on which both positive and negative events were summed regardless of their sign. Localization precision was also assessed from the repeated measurement of the center of the PSF. Center of mass calculation was used in both cases. The principle of this measurement is summarized in **Fig. 2a** and the precision results are displayed in **Fig. 2b**, along with the Cramér-Rao Lower Bound (CRLB) values for the experimental conditions used with the EMCCD camera. Note that the beads detected on the EMCCD exhibit lower number of photons per cycle on average due to the use of a 30:70 beamsliptter in the detection path. Overall, the event-based sensor precision was found to be on par with the EMCCD center of mass calculation, or slightly better. In particular, precisions below 10 nm are found in the typical levels of signals of SMLM fluorophores, and sub-5 nm precision is obtained with approximately 5000 photons, which is the level of signal emitted by many far red organic dyes such as Alexa Fluor (AF) 647. Precision tends to improve slightly with finer sensitivity values. Interestingly, experimental precision was found to be slightly better than the EMCCD CRLB, which we attribute to a very low level of background-induced events and read noise when working with an event-based sensor.

We furthermore characterized the linearity of the response, which is an important aspect for the quan-

bioRxiv preprint doi: https://doi.org/10.1101/2022.07.22.501162; this version posted July 24, 2022. The copyright holder for this preprint (which was not certified by peer review) is the author/funder, who has granted bioRxiv a license to display the preprint in perpetuity. It is made available under aCC-BY-ND 4.0 International license.

titativity of the output data. We used the same acquisition and processing as described in **Fig. 2a**, and we displayed the number of output events per period as a function of the number of incoming photons per period in **Fig. 2c**. As expected, the number of events recorded for a given input signal increases as the sensitivity gets finer (i.e. from low to high sensitivity). Interestingly, the relationship between the output and the input was found to be largely linear for all sensitivity levels investigated, and over a large range of input signal values (unlike the specifications given by the manufacturer). Only the data points above 20000 photons per period seem to deviate from the linear regime, but a signal at that level exceeds the typical conditions of SMLM acquisitions. We hypothesize that the output becomes more strongly logarithmic at higher levels of input signal, as this particular sensor has been originally designed to work at ambient light levels.

To further illustrate the capability of such a sensor for SMLM, we reconstructed and displayed the PSF obtained over one period in **Fig. 2d** for an input signal of 10000 photons and an integrated output signal of 1000 events approximately (with a high sensitivity). The PSF displays a very usual shape (as could be expected due to the linearity of the response with the input optical signal characterized previously), and a profile plots yields a width around w=190 nm (standard deviation), slightly above EMCCD values (w=170 nm, data not displayed).

After the characterization of the system with fluorescent beads, we set out to use the event-based sensor to detect single molecules, focusing on organic dyes typically used for dSTORM. We deposited AF647 dyes on a coverslip, immersed them in dSTORM buffer and illuminated them with typical dSTORM laser power density (see **Methods** section) to induce blinking. Acquisitions were performed with the event-based sensor, and frames reconstructed at Δt=10 ms are displayed in **Fig. 2e**. The blinking can be efficiently monitored—molecules exhibit a typical positive rising edge, followed by a few tens of ms without any signal, and finally a negative falling edge at the same position as the rising edge (similar to the output of beads with a square modulation displayed in **Fig. 1e**). Much like on beads, all the events in a localization regardless of their sign can be summed to reconstruct a PSF, as shown in **Fig. 2f**. Again, the PSF displays a very similar aspect to camera-based PSFs.

We also investigated the temporal behaviour of the fluorophore blinking, which is readily returned by the sensor output. This is displayed as positive and negative profiles in **Fig. 2g**. While some dyes have a very clear profile with well-defined rising and falling edges (the falling edge still displaying the trail mentioned previously) and few events in between, others display a very erratic behaviour, with a succession of multiple rising and falling edges, and seemingly intermediate levels of gray. This is consistent with the blinking regime observed on an sCMOS camera under the same illumination conditions and with an exposure time of 10 ms (data not displayed). Organic dyes under oxygen reduction buffers are known to have more complex photophysical behaviour than fluorescent proteins used for PALM or dyes used for DNA-PAINT, where the emission of the labels is closer to a clean square signal. We point out that, interestingly, event-based SMLM could provide an efficient way to both characterize these temporal emission fluctuations and image the dyes without any performance or information loss.

Event-based SMLM bioimaging

As organic dyes could be efficiently detected with our event-based single-molecule localization method, we then moved on to imaging fixed biological samples labelled with AF647. We prepared COS-7 cells and labelled the α-tubulin with AF647 (see **Methods** section). A dSTORM imaging buffer was used and the sample was illuminated with a laser beam at typical dSTORM power density (see **Methods**). Using a 50:50 beamsplitter in the detection path, we performed a simultaneous EMCCD and event-based acquisition.

2D SMLM images obtained with the event-based and the EMCCD sensors were found to be very sim-

bioRxiv preprint doi: https://doi.org/10.1101/2022.07.22.501162; this version posted July 24, 2022. The copyright holder for this preprint (which was not certified by peer review) is the author/funder, who has granted bioRxiv a license to display the preprint in perpetuity. It is made available under aCC-BY-ND 4.0 International license.

ilar at the scale of the whole field of view of 21x21 μm^2 (**Fig. 3a**), with the event-based localization image even yielding slightly more homogeneous localization densities over the field of view, especially in dense regions. At the nanometer length scale (**Fig. 3b**), the event-based detection performed on par or even outperformed the EMCCD, allowing to resolve the hollow core of the microtubules (see the cyan arrows and the corresponding profiles in **Fig. 3c**). Note that taking into account the diameter of the microtubules (30 nm) and the size of the antibody labelling (10 nm on each side), tha apparent diameter is expected to be around 50 nm (see [8, 18] for more information). While both the event-based center of mass detection and the EMCCD Gaussian fitting reveal the apparent hollowness of the microtubules, a simple center of mass calculation with the EMCCD fails to do so. We furthermore performed resolution assessments using the now well established Fourier Ring Correlation (FRC) method [36] throught the NanoJ-SQUIRREL Fiji plugin [37] (see **Methods** section). The results presented in **Supplementary Fig. 1** show an event-based resolution of 36 nm with a center of mass calculation and 30 nm with Gaussian fitting, very close to the reliable Gaussian fitting EMCCD resolution (28 nm), and significantly better than a simple center of mass calculation on the EMCCD data (50 nm). All the resolution measurements are summarized in **Supplementary Table. 1**. While using a dual-view detection setup is useful to monitor the acquisition in real time and to compare the final results, it is not necessary and it reduces the number of collected photons. To exploit the full potential of the event-based sensor, we performed an acquisition using a mirror in place of the beamsplitter cube, whose result is displayed in **Fig. 3d**. There again, the event-based SMLM ensures consistent localization performance over the whole ROI, and yields excellent precision that allows to resolve the microtubules apparent hollow core even more clearly, as shown on the profiles in **Fig. 3e**.

Our results so far clearly demonstrate the feasibility of SMLM bioimaging with an event-based vision sensor, which is able to perform on par with a conventional and more costly EMCCD camera due to its virtually non existent reading noise. Moreover, while very useful for classical SMLM imaging, our event-based method gives us access to supplementary information other than the position of detected molecules. To illustrate this, we used event-based sensing to extract photophysical properties of the fluorophores, namely the ON time (as defined in the section **Principle, optical setup and data display** as well as in **Fig. 2g**) and the total number of events counted in each localization—which increases approximately linearly with the total number of photons emitted by the molecule, as mentioned previously.

Fig. 3f displays super-resolved maps of the ON time and number of events detected for each molecule. The Gaussian shape of the illumination profile is clearly visible, and, as expected, both follow an inverse evolution—high ON times corresponds to molecules that are excited with low power, and therefore emit low numbers of photons (hence low numbers of events). A more quantitative assessment of this is provided in **Fig. 3g**, where both histograms are displayed in two different regions. In this acquisition, the ON time and the number of events only reveal the Gaussian shape of the illumination beam, but these quantities are often used in the literature to highlight chemical affinities or near-field optical effects at the molecular scale. One can cite for example the use of engineered DNA-PAINT strands and labels to perform high-specificity multi-species demixing (using the binding time and frequency, as well as the intensities collected in three different color channels) [38]. Examples of the use of the ON time and intensities in single-molecule nanophotonics include probing the changes in photophysical properties that fluorescent molecules undergo near a plasmonic gold surface or in a nanometric volume where the excitation field is vastly enhanced [39, 26]. One interesting use of event-based SMLM could be demixing of simultaneous multicolor blinking sequences, assigning each molecule a color based on its ON time or photophysical behaviour without the need for adapting the acquisition to resolve such variations. Such a demixing could be done either using user-defined criteria or through a deep learning algorithm.

bioRxiv preprint doi: https://doi.org/10.1101/2022.07.22.501162; this version posted July 24, 2022. The copyright holder for this preprint (which was not certified by peer review) is the author/funder, who has granted bioRxiv a license to display the preprint in perpetuity. It is made available under aCC-BY-ND 4.0 International license.

Event-based high density imaging

In order to exploit the unique capabilities of event-based sensors for single-molecule imaging, we use it in a regime where the density of PSFs is very high and their overlap significantly compromises the localization performance of frame-based acquisitions. The density of the PSFs in each frame results from the combination of several factors, in particular the density of the protein of interest, the density of the fluorescent labels and the blinking behaviour of the molecules. This can happen in particular in dSTORM experiments, where the density of molecules is usually difficult to control. Still, this is a more general problem, even when working with PALM or DNA-PAINT labels that allow more flexible control of the density of active PSFs. Indeed, independently of the labelling strategy, the most common approach when using frame-based cameras is to adapt the density of active fluorophores to the most dense structures in the field of view to have sparse PSFs in those regions. This, however, implies that the acquisition duration has to be increased to properly sample the less dense structures. However, in some cases such as acquisitions in living samples, this may not even possible, resulting in under-sampled structures. Very few techniques are available to tackle such situations. While SOFI [40, 41] yields consistent performance over a large range of molecule densities, it is not intrinsically a single-molecule approach, therefore it is not very well suited for quantitative applications such as molecule counting measurements. Other single-molecule approaches to process dense PSFs may require cumbersome procedures of deconvolution [42] or deep learning agorithms [43].

We propose to take advantage of the spatio-temporal resampling capabilities of the event-based sensors to perform high density imaging. From a conceptual point of view, one can consider the case where the blinking dynamic is low but the density of molecules sufficiently high to induce significant overlap—for example in a PALM experiment where the excitation power is low but the photoactivation rate high. In such situations where regular frame-based acquisitions would fail no matter what frame rate is chosen, the event-based sensor, on the contrary, would be able to detect (and localize) a molecule that becomes fluorescent or photobleaches among many others that maintain a constant level of emission. The same reasoning stands for dSTORM experiments where the switching rate is too low (when the excitation power is not sufficient for example) or simply where the density of labels is too high (such as at the beginning of the pumping phase, which is often discarded, leading to a loss of time and data).

To illustrate this principle, we performed acquisitions where a very dense layer of 488-nm-excitable fluorescent beads is deposited on a coverslip, alongide a few, sparse 647-nm-excitable fluorescent beads. We used a multiband filter to excite and collect both wavelength channels, and we excited with a continuous 488 nm laser and a square-modulated 638 nm laser at 10 Hz. The 488 nm beads thus mimic dense static background with overlapping PSFs, and the 647 nm beads imitate the effect of a few molecules turning on or off on that background. Again, we used a 50:50 beamsplitter cube in the detection path to compare the performance of both imaging modalities. The results presented in **Fig. 4a** yield EMCCD frames where most 647 nm beads cannot be localized with usual approaches. In contrast, the event-based reconstructed frames contain almost no trace of the static background, and reveal very clearly the modulated beads even in the cases where they are not visible to the naked eye in the EMCCD frame. Note in particular that, while beads 1 and 2 are clearly visible on the EMCCD image, beads 3 and 4 would be more challenging to localize due to the overlapping neighbouring PSFs. Finally, beads 5 and 6 are almost impossible to localize with standard processing algorithms. All of them are clearly visible and localizable on the event-based image.

Having validated the principle with such a first simple experiments, we moved on to real blinking acquisitions on biological samples. We therefore imaged a fixed COS-7 cell labelled with anti-α-tubulin primary and AF647-conjugated secondary antibody as in the section **Event-based high density imaging** and in **Fig. 3**, which we excited with a relatively high power density in a standard dSTORM buffer. However, instead of waiting for the end of the pumping phase, when the molecule density starts to become sparse, we started the acquisition at the same time as the excitation. Furthermore, we chose a region where the microtubules are closely interwoven and the PSF density is thus

bioRxiv preprint doi: https://doi.org/10.1101/2022.07.22.501162; this version posted July 24, 2022. The copyright holder for this preprint (which was not certified by peer review) is the author/funder, who has granted bioRxiv a license to display the preprint in perpetuity. It is made available under aCC-BY-ND 4.0 International license.

high. Using again a 50:50 beamsplitter cube, we compared the performance of an EMCCD-based and the event-based SMLM methods over the course of a short 250 s acquisition (during which the density of PSFs remains high).

The event-based processing code was adapted to resample the data on shorter time scales. More specifically, frames were generated from either the positive events only with a time bin of Δt=10 ms, and the localization was subsequently performed on the corresponding positive-only events within a short time range $[T_0 - 30\text{ ms}, T_0 + 30\text{ ms}]$ centered around the frame timestamp. By running the processing on such a fine time scale, we expect to extract only the moment when a molecule turns on while its neighbours maintain a roughly constant level of emission. Then, a similar processing was performed to extract the moment when the molecules turn off. Even though this loses track of the link between the rising edge and the falling edge for each molecule and thus prevents the extraction of the ON time, it does retain the quantitative aspect of the measurement (each rising edge generates one positive localization, and each falling edge generates one negative localization), so molecules could still be counted. On the other hand, the EMCCD acquisition was carried out with a 30 ms exposure time and processed with a standard algorithm. It should be noted here that the exposure time is below the typical ON times of the dyes, which implies that the density of PSFs per frame is not very sensitive to the exposure time, and is on the contrary mostly determined by the density of the target protein, the density of labelling as well as the global fraction of active dyes (in other words the pumping rate and elapsed pumping time).

Supplementary Fig. 2 shows both an ROI of an EMCCD frame, where the PSFs are found to be dense enough to overlap, and an event-based generated frame of the positive only events in a Δt=10 ms time bin. On that frame (used only for the PSF detection), the density of molecules seems vastly reduced compared to the EMCCD frame, which means that although many neighbouring molecules are in an ON state, the variations of the signal are sparse enough to be spotted individually. The last frame shows all the positive events in the $[T_0 - 30\text{ ms}, T_0 + 30\text{ ms}]$ range around the frame, revealing levels of signal and noise a priori sufficient to allow localization.

Running the localization workflow on the whole 250 s long event-based dataset produced a strikingly well-sampled 2D SMLM image (**Fig. 4b**). As expected, the image exhibits a very uniform resolution, with little loss of sampling density or resolution either in dense areas or at the edges of the field of view. A more detailed view is presented in **Fig. 4c**, which reveals overall very satisfactory resolution performance. While the resolution is not as good as in the optimal case presented in **Fig. 3d** (the apparent hollow core of the microtubules is not visible here), it is very satisfactory given the suboptimal acquisition conditions—50 % of the photons only, 4 minutes of acquisitions compared to usual times around 20–30 minutes in dSTORM experiments, high density of PSFs and each localization containing only the positive or only the negative events (leading to an immediate $\sqrt{2}$ loss in resolution).

Overall, we consider that given these challenging imaging and processing conditions, the event-based SMLM performs very well both with center of mass calculation (**Fig. 4c** left) and Gaussian fitting (super-resolved image not displayed), as the tubulin filaments are well resolved and do not exhibit significant undersampling. This is even more striking when the results are compared to those obtained over the same area with a standard processing from the EMCCD acquisitions. **Fig. 4c** shows an undersampled 2D SMLM image with a Gaussian fitting EMCCD-based processing that does not allow to properly distinguish a certain number of tubulin filaments, especially in dense areas. A more basic center of mass algorithm run from the EMCCD frames yielded even more catastrophic results, with resolutions hardly better than the diffraction limit in dense areas. A quantitative assessment of the image resolution using FRC is provided in **Supplementary Table. 1** and in **Fig. 4d**. The resolution was found to be 64 nm for event-based SMLM (both for center of mass calculation and Gaussian fitting), compared with 92 nm and 136 nm for EMCCD-based SMLM with Gaussian fitting and center of mass calculation, respectively. The resolution maps presented in **Fig. 4d** highlight not only the better overall performance of event-based SMLM, but also the reliability of the resolution,

bioRxiv preprint doi: https://doi.org/10.1101/2022.07.22.501162; this version posted July 24, 2022. The copyright holder for this preprint (which was not certified by peer review) is the author/funder, who has granted bioRxiv a license to display the preprint in perpetuity. It is made available under aCC-BY-ND 4.0 International license.

which is much more uniform than with EMCCD acquisitions.

These results provide a convincing proof of principle of how the spatio-temporal resampling properties inherent in event-based SMLM can be used to improve localization performance compared to classic scientific cameras without resorting to complex processing workflows. The performance could be further enhanced by refining the processing pipeline. In particular, we believe that it would be possible to assess the local (in space and in time) density of molecules to adapt the processing conditions. For example, the time base and the PSF localization area could be relatively large in areas with low density to allow detection of both the rising edge and the falling edge, while denser areas could be processed with the high density algorithm, associated with a fine time base and dissociation of the positive and negative events. We expect such a more subtle type of algorithm to improve both the processing time and the localization performance, and potentially the quantitativity at the same time. This is conceptually reminiscent of previous works such as [44], where the size of the spatial range available for PSF shaping is adapted in real time according to the density of molecules (which varies in time during the acquisition), or [33], where the acquisition speed is adapted in real time so that it allows, recording of data at a sufficient rate while saving storage and processing power. Nevertheless, a fundamental advantage of event-based SMLM is that the sensor records data as fast as it can, which means that no prior knowledge about the acquisition behaviour is needed, and that workflow refinements are inherently processing-based. Another advantage is that, while the exposure time of cameras can be varied in time, all the chip is constrained with the same exposure time—by contrast, all event-based processing parameters can be varied along spatial dimensions as well.

Discussion

With this work, we have demonstrated, for the first time to our knowledge, the use of novel neuromorphic vision sensors for SMLM super-resolution fluorescence imaging. Besides its more affordable price than conventional EMCCD or sCMOS scientific cameras, the unique characteristics of event-based sensors make them perfectly suited for detecting sparse events in space and time, incidentally the working principle of SMLM. With our event-based SMLM approach, we have obtained dSTORM super-resolution images of the α-tubulin cytoskeleton network of COS-7 cells labeled with AF647 with a spatial resolution on par with the state-of-the-art approach using an EMCCD camera. We have also seen that the event-based sensor provides access to quantitative information like the ON time and the number of events of the detected single fluorophores. Importantly, event-based SMLM opens new avenues for single-molecule applications where classical frame-based cameras are unable to perform, like we have shown in the case of high-density acquisitions with overlapping PSFs.

The range of applications of event-based sensing is a priori very broad since it is very well suited to the extraction of the dynamics of biological processes. In the context of fluorescence microscopy, it could be especially useful to monitor processes that exhibit a wide range of dynamic scales. An extreme example would be that of a system that would not evolve for several hours before suddenly exhibiting dynamics in the millisecond range—such a system would be extremely challenging to monitor with frame-based approaches due to the necessity to use an exposure time short enough to sample the motion while keeping realistic data volume and processing times. While that example may seem purely theoretical, certain phenomena exhibit an extreme range of dynamic scales. One can cite colloidal glass transition, which is associated to time scales ranging over more than ten orders of magnitude, with large spatial variations of dynamics [45, 46].

In the framework of SMLM, we found event-based detection to be extremely useful in some cases. A simple implementation of event-based SMLM readily unlocked resolutions and densities on par with state-of-the-art scientific camera-based approaches. If one considers that the key to super-resolution is the control and acquisition of some on/off behaviour of the fluorescent labels, which is a common view in the community [47], then it appears that event-based sensors are particularly well suited for

bioRxiv preprint doi: https://doi.org/10.1101/2022.07.22.501162; this version posted July 24, 2022. The copyright holder for this preprint (which was not certified by peer review) is the author/funder, who has granted bioRxiv a license to display the preprint in perpetuity. It is made available under aCC-BY-ND 4.0 International license.

the purpose of blinking-based imaging of continuous structures since it essentially detects only the on and off transitions while discarding all the rest of the signal and the associated noise in the process. In the same situation, frame-based approaches usually run extra steps aiming at removing static signal or at extracting dynamic components such as median temporal filtering or blink linking over several frames to identify the same position detected in several consecutive frames and to merge it into one localization to improve the quantitativity and maximize the number of photons (in contrast, event-based SMLM ideally uses exactly one rising and one falling edge per blinking cycle), which may add complexity and noise or errors. Furthermore, these steps usually fail under challenging imaging conditions such as when the density of PSFs is high. On the contrary, we demonstrated that event-based SMLM is largely unaffected under these conditions, which we attribute to both its ability to extract the useful information only, as well as the possibility to easily perform efficient temporal resampling at the processing step to reduce the spatio-temporal density of signal to manageable levels.

We expect that event-based SMLM could benefit from several improvements, both from the point of view of the optical design and that of the processing software. Clever strategies could be implemented to adapt the spatio-temporal analysis (i.e. the area of the PSF analysis and the processing time base) to the local density (in space and time) of the output signal, which is essentially a sparse matrix. This would probably lead to an increase in calculation speed and localization performance. Other more specific improvements could be made, like using better suited PSF models for the position calculation such as cubic spline [48] or deep learning-generated bases of experimental PSFs [49, 50, 43]. A noise model for the event-based sensing that would provide an estimation of the CRLB would be a very useful addition to this.

Given the high density imaging capabilities shown in **Fig. 4**, we also hypothesize that event-based SMLM could be used for quantitative applications in dSTORM since the pumping phase needs not be discarded, and the molecules blinking during that phase can be effectively counted. In other studies where the quantitative aspect is not as important as the acquisition speed (such as for live imaging or for high content screening), it could also benefit dSTORM and PALM experiments by allowing faster acquisitions—well sampled dSTORM images of dense structures can be obtained in a few minutes only as demonstrated previously, and PALM experiments could be carried out using higher photoactivation powers without compromising the PSF sparsity criterion. For this purpose, the use of an image quality assessment method such as [37] could provide useful information about the minimum acquisition time to obtain the desired image quality.

Another very different set of applications where event-based SMLM may excel could be modulated excitation techniques, where a controlled time-modulated illumination is applied and the fluorescence signal is demodulated to extract a parameter of interest. This can be the excitation wavelength in simultaneous multicolor experiments [51], the lateral position [52, 53], the axial position [5, 54] or the orientation of the dipole associated with the molecule [55] (non exhaustive list). In all these cases, however, the temporal aspect is crucial to the performance. While some approaches apply very low exposure times at the cost of low signal and high sensitivity to intensity fluctuations, others use pre-demodulated detection paths in combination with fast electrical switching between the channels, which brings experimental complexity and reduces the effective field of view. We hypothesize that given their speed event-based sensors should be able to record the temporal modulated output without inducing much noise or reducing the signal level by splitting the useful photons. Therefore, event-based sensing could readily capture the dynamics of the response, which could then be effectively analyzed without the need for temporal sampling.

bioRxiv preprint doi: https://doi.org/10.1101/2022.07.22.501162; this version posted July 24, 2022. The copyright holder for this preprint (which was not certified by peer review) is the author/funder, who has granted bioRxiv a license to display the preprint in perpetuity. It is made available under aCC-BY-ND 4.0 International license.

Acknowledgements

We acknowledge Christian Hubert as well as Tual Monfort and Olivier Thouvenin for their invaluable help with conceiving the project, as well as for hardware loan. We also thank Margoth Córdova-Castro, Vittore Scolari, Antoine Coulon, Sandrine Lévêque-Fort and Emmanuel Fort for fruitful discussions and feedback.

Author contributions

C.C. and I.I. conceived the project. C.C. designed the optical setup and performed the acquisitions, processing and data analysis. C.S. prepared the fixed cells samples and C.C. performed the immunolabelling. All authors contributed to writing the manuscript.

Competing financial interests

The authors declare no competing interest.

bioRxiv preprint doi: https://doi.org/10.1101/2022.07.22.501162; this version posted July 24, 2022. The copyright holder for this preprint (which was not certified by peer review) is the author/funder, who has granted bioRxiv a license to display the preprint in perpetuity. It is made available under aCC-BY-ND 4.0 International license.

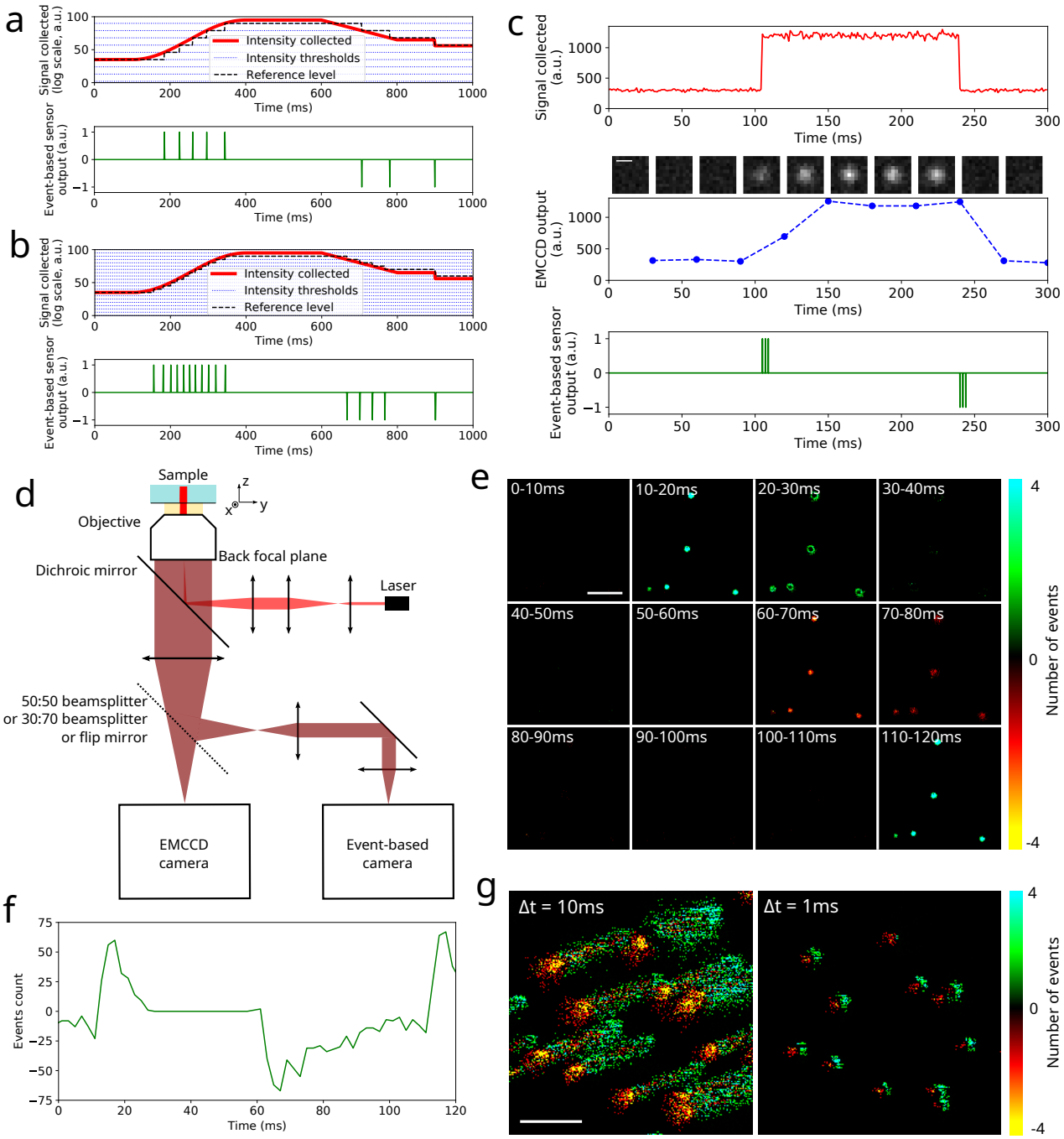

Figure 1: Principle of the event-based detection. **a** Description of the working principle of a pixel in an event-based sensor. A given optical intensity signal $I(t)$ is assumed, the sensitivity threshold B is set to an arbitrary value. The reference value is also displayed, as well as the response from the pixel. **b** Influence of the sensitivity on the output signal for the same $I(t)$ as in **a**, but B is lower (i.e. the detection is more sensitive). As a result of the sensitivity change, the the number of events generated for the same signal is higher. **c** Comparison of the responses produced by a scientific camera and an event-based sensor. The top row shows a theoretical $I(t)$ profile emitted by a fluorescent molecule turning on and then off, the middle row is the signal acquired by an ideal camera working at a 30 ms exposure time (the corresponding frames are displayed above the graph), and the bottom row displays the signal returned by an event-based sensor with arbitrary sensitivity.

bioRxiv preprint doi: https://doi.org/10.1101/2022.07.22.501162; this version posted July 24, 2022. The copyright holder for this preprint (which was not certified by peer review) is the author/funder, who has granted bioRxiv a license to display the preprint in perpetuity. It is made available under aCC-BY-ND 4.0 International license.

Figure 1: d Optical setup used for the single-molecule experiments. A laser produces a Gaussian excitation beam. The detection path comprises two detectors: and EMCCD camera and an event-based sensor. We use switchable deflectors to alternate between the two detection paths: we use either a 50:50 beamsplitter, a 30(EMCCD):70(event-based) beamsplitter, a mirror or nothing. More details are available in the **Methods** section. **e** Frames generated from the events acquired in an experiment where 200 nm fluorescent beads on a coverslip are excited with a square pulsed excitation with a period of 100 ms. The frames are generated with a time bin of Δt = 10 ms. The color codes the number of events in each pixel, with respect to the polarity of the events detected (positive or negative). The time limits are written for each frame. **f** Event time profile extracted from a single bead from **(e)** with a Δt = 2 ms time bin. The number of events represented corresponds to the sum of all the pixels over the PSF. **g** Frames generated at different time bins from an acquisition of 40 nm fluorescent beads deposited on a coverslip while the stage is translated from the bottom left to the top right to simulate molecule motion. From the same event list, frames are generated at Δt = 10 ms (left) and Δt = 1 ms (right). Scale bars: 0.5 µm (**c**), 5 µm (**e**), 5 µm (**g**).

bioRxiv preprint doi: https://doi.org/10.1101/2022.07.22.501162; this version posted July 24, 2022. The copyright holder for this preprint (which was not certified by peer review) is the author/funder, who has granted bioRxiv a license to display the preprint in perpetuity. It is made available under aCC-BY-ND 4.0 International license.

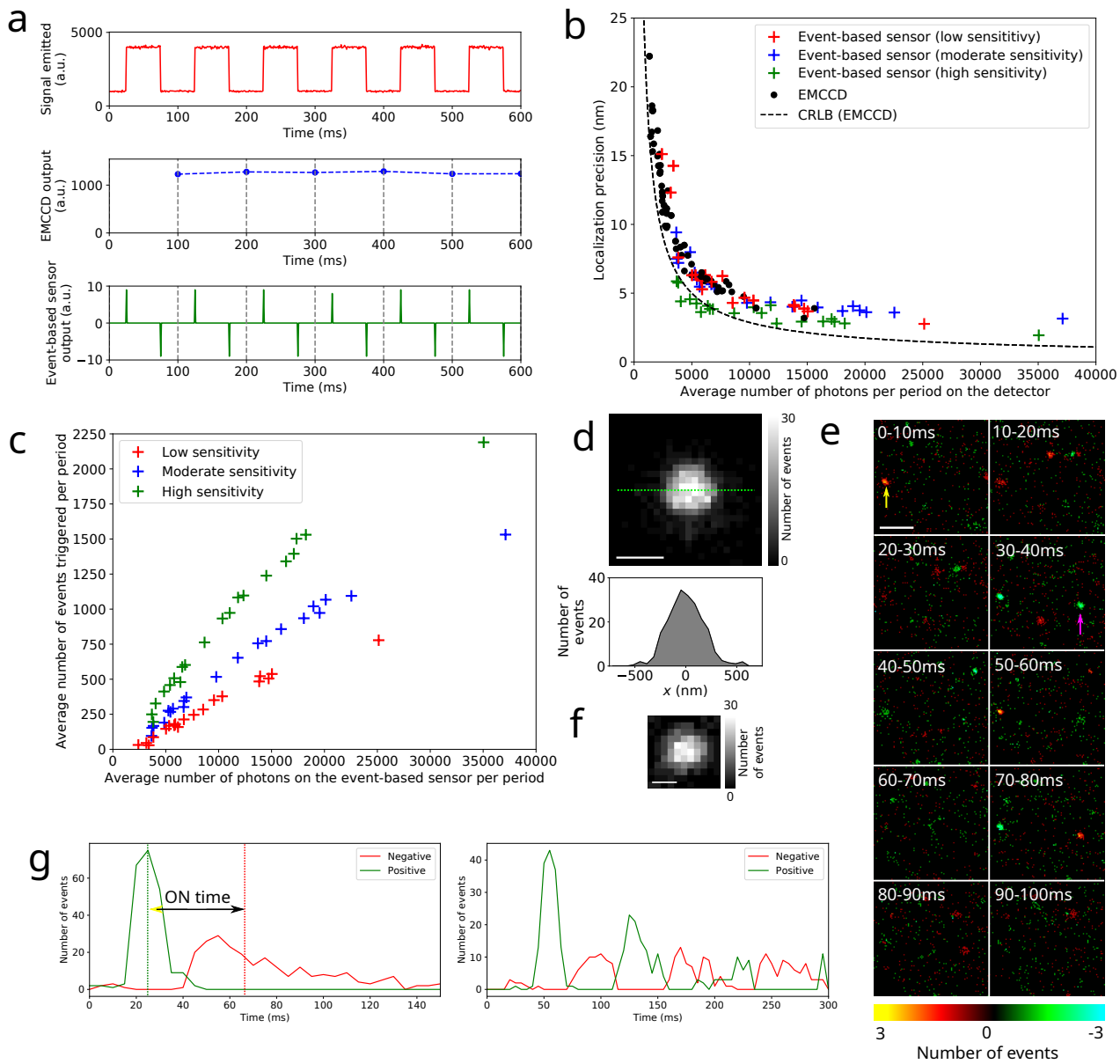

Figure 2: Single molecule localization and characterization of the performance. **a** Schematic of the experiment used to measure the localization precision. Fluorescent beads deposited on a coverslip are illuminated with a square modulated laser, therefore $I(t)$ has a square modulated profile. The EMCCD exposure time is set to exactly one period, so the signal is constant over all the frames (with the exception of the photon noise). The event-based sensor detects the rising and falling edges, and all the events in one period are pooled to compute the center of mass position. **b** Localization precision results displayed as a function of the number of photons incoming on each of the detectors (EMCCD or event-based sensor) per period (calculated from the number of photons detected on the EMCCD taking into account the 30:70 ratio). The results for the event-based sensor are displayed for different levels of sensitivity (i.e. different values of B). The CRLB curve corresponding to the EMCCD detection is also shown. **c** Linearity of the response, shown for different levels of sensitivity. The total number of events detected per period is displayed as a function of the number of photons incoming on the event-based sensor per period. Note the quasi-linearity of the response in this signal range. **d** PSF reconstructed by summing the events (regardless of their sign) detected over one period of 100 ms (top) for the same bead. An x profile along the green dashed line is plotted at the bottom.

bioRxiv preprint doi: https://doi.org/10.1101/2022.07.22.501162; this version posted July 24, 2022. The copyright holder for this preprint (which was not certified by peer review) is the author/funder, who has granted bioRxiv a license to display the preprint in perpetuity. It is made available under aCC-BY-ND 4.0 International license.

Figure 2: **e** Frames reconstructed with Δt = 10 ms from a sample of AF647 deposited on a glass coverslip excited with a continuous laser in a dSTORM buffer to induce blinking. Note that this data display reveals very different blinking behaviours from one molecule to the other—the molecule indicated with a yellow arrow undergoes multiple blinking events in a quick succession while that indicated by a magenta arrow exhibits a much simpler behaviour with essentially one rising edge and one falling edge. **f** PSF reconstructed from all the events in one AF647 blinking event. The data is taken from the same acquisition as in **e**, and the events are summed regardless of their sign. **g** Two time profiles plotted for different AF647 molecules in the same acquisition as **e**. The one on the left shows a simple blinking profile, which allows the calculation of the ON time, defined as the difference of the mean time of the negative events (moment when the molecule turns off) and the the mean time of the positive events (moment when the molecule turns on). The profile on the right, on the contrary, displays a complex behaviour with multiple blinking events. Scale bars: 500 nm (**d**), 2 µm (**e**), 250 nm (**f**).

bioRxiv preprint doi: https://doi.org/10.1101/2022.07.22.501162; this version posted July 24, 2022. The copyright holder for this preprint (which was not certified by peer review) is the author/funder, who has granted bioRxiv a license to display the preprint in perpetuity. It is made available under aCC-BY-ND 4.0 International license.

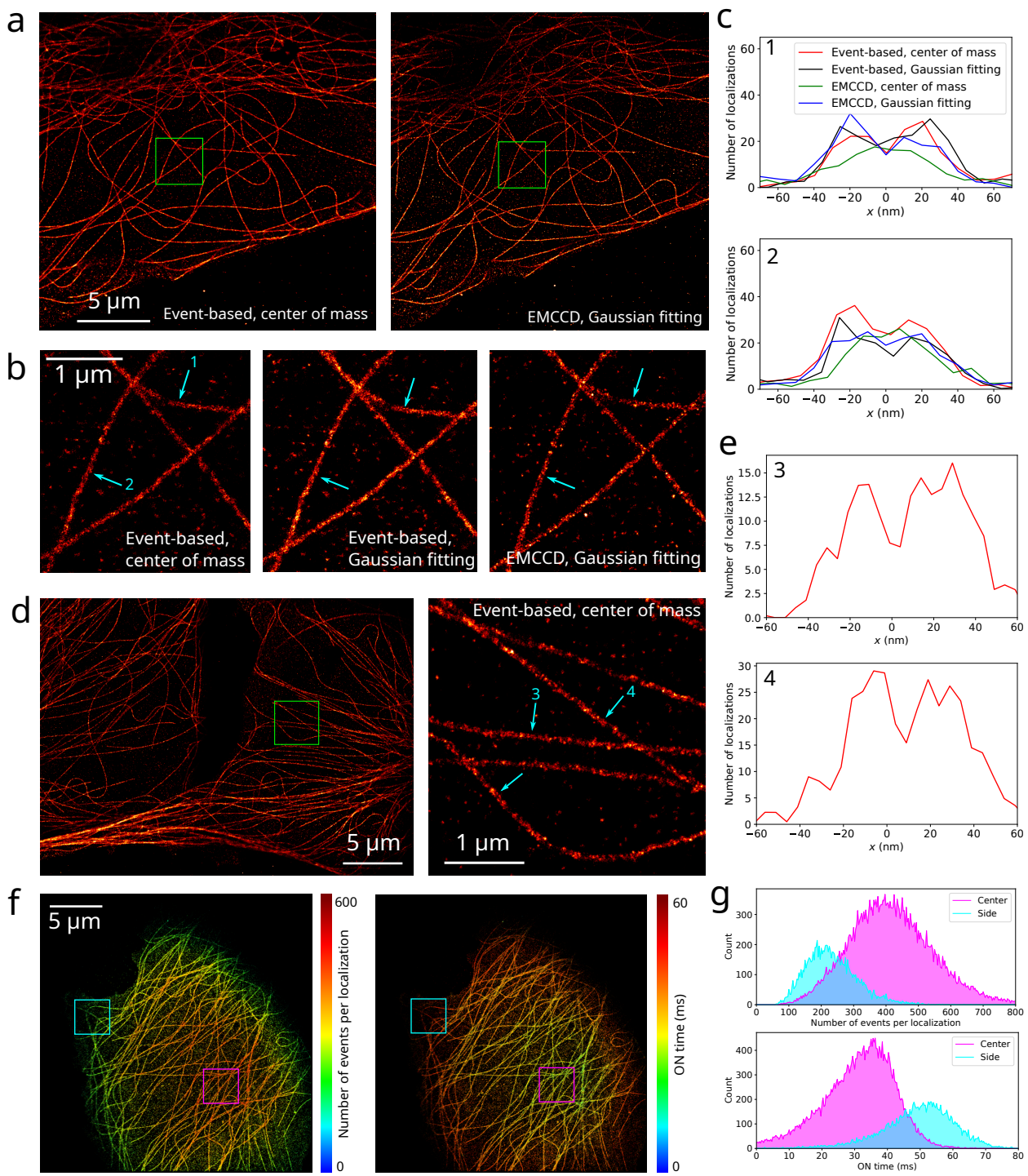

Figure 3: Imaging of fixed COS-7 cells labelled with AF647 against α-tubulin (see the **Methods** section for more information). **a** Simultaneous 2D SMLM image (the density of molecules is color-coded) obtained with the event-based sensor and the EMCCD camera using a 50:50 beamsplitter in the detection path. **b** Zoom on the region of **a** indicated with a green square. We compare the resolution obtained with the event-based sensor (localization performed by center of mass calculation or Gaussian fitting) and with the EMCCD camera (localization performed by Gaussian fitting; center of mass was calculated but is not displayed). **c** Molecule density profiles plotted perpendicular to the microtubules 1 and 2 in **b**. **d** 2D event-based SMLM image obtained with 100 % of the photons incoming on the event-based sensor. A zoom on the region indicated with a green square is also shown. **e** Molecule density profiles plotted perpendicular to the microtubules 3 and 4 in **d**. **f** Maps of the number of events per localization and of the ON time (color-coded values) for a different acquisition. **g** Corresponding histograms displayed for the two regions indicated with cyan and magenta squares. Scale bars: 5 µm (**a**, **d** left, **f**), 1 µm (**b**, **d** right).

bioRxiv preprint doi: https://doi.org/10.1101/2022.07.22.501162; this version posted July 24, 2022. The copyright holder for this preprint (which was not certified by peer review) is the author/funder, who has granted bioRxiv a license to display the preprint in perpetuity. It is made available under aCC-BY-ND 4.0 International license.

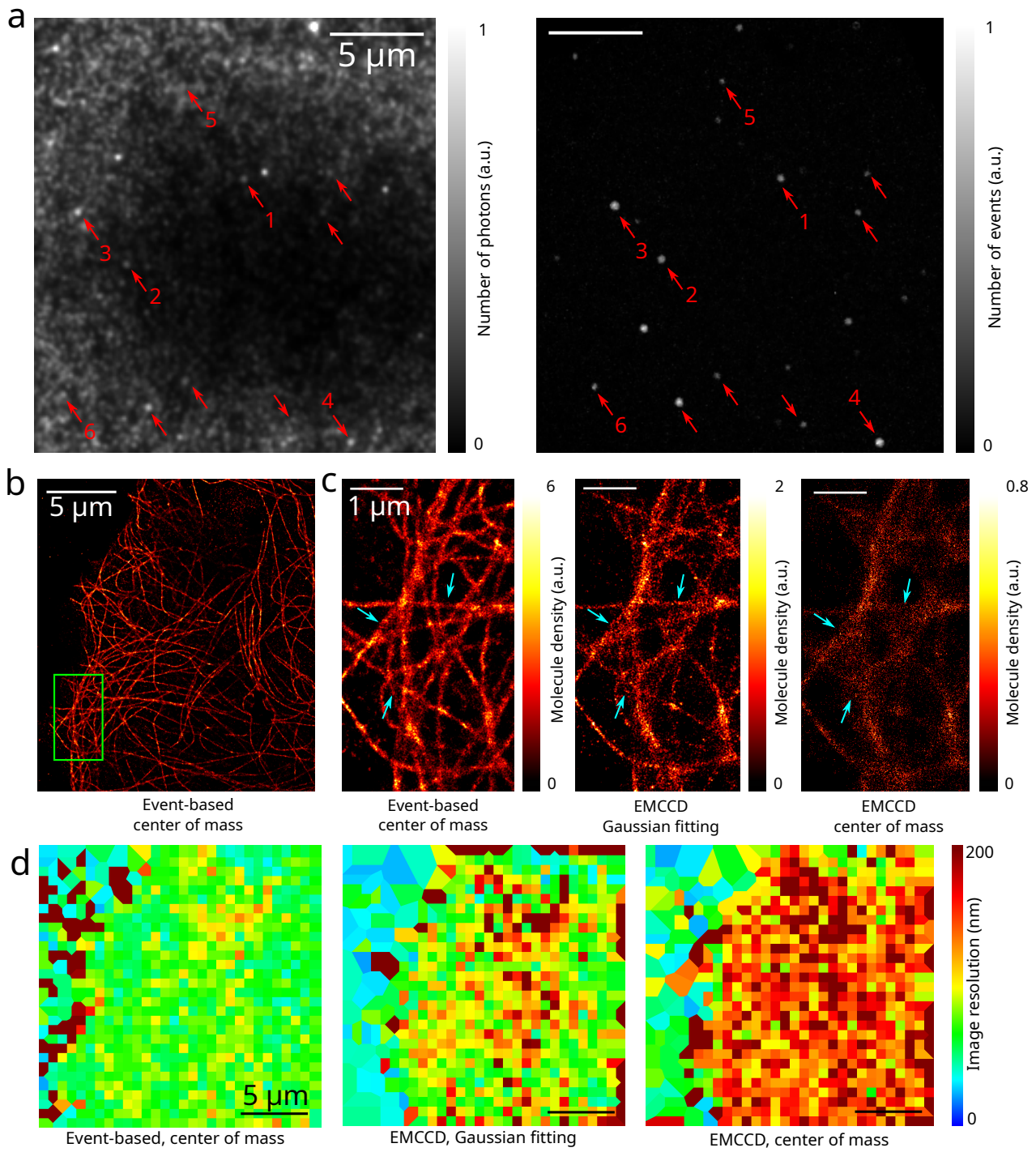

Figure 4: High density imaging. **a** Images of dense 488 nm fluorescent beads illuminated with continuous 488 nm excitation and sparse 647 nm beads excited with square modulated 638 nm excitation, using a multiband beamsplitter to collect both wavelength channels, and with a 50:50 beamsplitter between the two sensors. Left: Integrated signal (i.e. sum of all the frames) obtained with the EMCCD camera; right: integrated signal (i.e. sum of all the events) obtained with the event-based sensor. Some of the 647 nm beads are indicated with red arrows. **b** Event-based SMLM image (the density of localizations is color-coded) obtained from the same 250 s long acquisition. **c** Zoom on the area indicated with a green rectangle in **b**, for the same 250 s long acquisition with simultaneous event-based sensor and EMCCD detections. The SMLM images are shown for different localization conditions: from the event-based sensor data with center of mass calculation (left), from the EMCCD data with Gaussian fitting (center), and center of mass calculation (right). Note the different scales of the colorbars.

bioRxiv preprint doi: https://doi.org/10.1101/2022.07.22.501162; this version posted July 24, 2022. The copyright holder for this preprint (which was not certified by peer review) is the author/funder, who has granted bioRxiv a license to display the preprint in perpetuity. It is made available under aCC-BY-ND 4.0 International license.

Figure 4: d FRC resolution maps calculated on the area displayed in **b** for the different localization methods tested. Scale bars: 5 µm (**a**, **b**, **d**), 1 µm (**c**).

bioRxiv preprint doi: https://doi.org/10.1101/2022.07.22.501162; this version posted July 24, 2022. The copyright holder for this preprint (which was not certified by peer review) is the author/funder, who has granted bioRxiv a license to display the preprint in perpetuity. It is made available under aCC-BY-ND 4.0 International license.

Methods

Optical setup. A schematic of the optical setup used is presented in **Fig. 1d**. We used a custom-built microscope with a RM21 body and a MANNZ micro- and nano-positioner. The illumination and fluorescence collection was done with a Nikon 100x 1.49NA APO TIRF SR oil immersion. The excitation was performed thanks to a 638 nm laser (LBX-638-180, 180 mW, Oxxius) and a 488 nm laser (LBX-488-100, 100 mW, Oxxius) with a 405 nm laser for pumping (LBX-405-50, 50 mW, Oxxius). A full multiband filter set (LF405/488/561/635-A-000, Semrock) was used. The excitation consisted of a standard vertical Gaussian beam without any scanning, speckle removal or optical sectioning. The fluorescence was sent in the detection module and recorded on the EMCCD camera (iXon Ultra 897, Andor) and/or on the event-based sensor (EVK V2 Gen4.1, Prophesee). Both sensors had their focal planes approximately matched (below 200 nm difference). We used afocal doublets to adjust the pixel sizes to 107 nm (EMCCD) and 65 nm (event-based sensor) in the object plane. Depending on the acquisition, we placed different elements in the detection path thanks to a flip platform—either a 50:50 non-polarizing beamsplitter (Thorlabs), or a a 30(EMCCD):70(event-based sensor) non-polarizing beamsplitter (Thorlabs), or a plane mirror (Thorlabs) to deflect all the signal on the event-based sensor, or nothing to collect all the fluorescence on the EMCCD camera.

Fluorescent beads sample preparation (Fig. 1g and Fig. 2b–d). The sample was prepared by diluting dark red (660/680) 40 nm fluorescent beads (F10720, Thermo Fisher) with a dilution factor of 10^{-7} in phosphate buffered saline (PBS) and allowing them to deposit on a coverslip.
The sample used for **Fig. 1e–f** was prepared by diluting dark red (660/680) 200 nm fluorescent beads (F8807, Thermo Fisher) with a dilution factor of 10^{-3} in PBS and allowing them to deposit on a coverslip.
The sample used for **Fig. 4a** was prepared by diluting dark red (660/680) 40 nm fluorescent beads (F10720, Thermo Fisher) with a dilution factor of 8×10^{-8} and yellow-green (505/515) 40 nm fluorescent beads (F10720, Thermo Fisher) with a dilution factor of 8×10^{-6} in PBS and allowing them to deposit on a coverslip.

Alexa Fluor 647 on a coverslip sample preparation (Fig. 2e–g). The sample was prepared by depositing 1.5 µl of the initial solution of AF647 goat anti-mouse antibody (A21237, Thermo Fisher), allowing 5 minutes for the molecules to deposit before rinsing with H_2O and adding dSTORM buffer. The buffer was composed of 100 mg/ml glucose, 3.86 mg/ml MEA, 0.5 mg/ml glucose oxidase and 1.18 µl/ml catalase in PBS. The sample was illuminated with a 638 nm continuous excitation at an irradiance of 5 kW/cm^2.

Biological samples preparation. African green monkey kidney cells (COS-7) were cultured at 37°C and 5 % CO_2 in DMEM medium containing glutamax (Gibco No. 31966-047), 10 % fetal bovine serum (FBS, Gibco No. A3840401) and 50 U/ml penicillin and 50 µl/ml streptomycin (Gibco No. 15140-148). For experiments, cells were plated on 25 mm diameter glass coverslips (type 1.5) placed in six well plates containing culture medium with 2 % FBS at low density, and fixed on the following day in 0.1 M sodium phosphate buffer (PB), pH 7.4, containing 4 % paraformaldehyde (PFA), 0.2 % glutaraldehyde, 1 % sucrose, at 37°C for 10 minutes, followed by three rinses in PBS. Cells were permeabilized with PBS containing 0.1 % Triton X-100 for 10 minutes and rinsed three times with PBS prior to immunolabelling.
For the labelling, the cells were incubated for 1 hour at 37°C with 1:300 mouse anti-α-tubulin antibody (Sigma Aldrich, T6199) in PBS + 1 % BSA. This was followed by three washing steps in PBS + 1 % BSA, incubation for 45 minutes at 37°C with 1:300 goat anti-mouse AF647 antibody (Life Technologies, A21237) diluted in PBS 1 % BSA and three more washes in PBS. Finally, the cells were post-fixed with 3.6 % formaldehyde for 15 min in PBS. The cells were washed in PBS three times and then reduced for 10 minutes with 50 mM NH_4Cl (Sigma Aldrich, 254134), followed by three additional washes in PBS.

Localization precision and response linearity measurement (Fig. 2b–c). Acquisitions were performed on fluorescent beads deposited on a coverslip using a square modulated 638 nm excitation

bioRxiv preprint doi: https://doi.org/10.1101/2022.07.22.501162; this version posted July 24, 2022. The copyright holder for this preprint (which was not certified by peer review) is the author/funder, who has granted bioRxiv a license to display the preprint in perpetuity. It is made available under aCC-BY-ND 4.0 International license.

with a frequency of 10 Hz, a duty cycle of 0.5 and a minimum laser output of 0 mW. Using a 30:70 (camera:event-based sensor) non-polarizing beamsplitter, acquisitions were captured simultaneously on the camera (100 ms exposure) and on the event-based sensor with various sensitivity values. Event-based frames were generated by summing all the events in Δt =100 ms time bins regardless of their sign. The positions were calculated using a center of mass calculation on both the event-based reconstructed and the camera-acquired frames. Positions were drift-corrected using a direct cross-correlation algorithm. A simple clustering algorithm was used to determine the localization precision from the calculated positions as well as the average number of photons/events for each bead. A total of 1000 frames were included in the statistics. Finally, a colocalization algorithm was used to match the camera-based and the event-based bead positions in order to compare the performances of both methods. The average number of photons per cycle on the camera was calculated for each bead from the camera localization results, and this number was subsequently used to calculate the average number of photons per cycle on the event-based sensor for each bead by applying a ratio corresponding to the beamsplitter ratio (experimentally measured to be 1:2.38).

Standard density biological experiments (Fig. 3). EMCCD acquisitions were done with a 30 ms exposure time and a gain of 100, and event-based was done with thresholds corresponding to the level of sensitivity called 'high' in the characterization. The detection path used either a 50:50 non-polarizing beamsplitter cube or a mirror to send all the photons on the event-based sensor. Both sensors were not synchronized but dual-view acquisitions were started and stopped simultaneously. We used a dSTORM buffer composed of 100 mg/ml glucose, 3.86 mg/ml MEA, 0.5 mg/ml glucose oxidase and 1.18 µl/ml catalase in PBS and a 638 nm continuous excitation with an irradiance of 5 kW/cm^2. After a pumping phase of a few minutes, the acquisitions were started and stopped after 25 minutes. A low power continuous 405 nm excitation was also added during the second half of the acquisition to increase the density of detections.
EMCCD frames were processed using a wavelet algorithm to detect the PSFs and each PSF was localized on a ± 4 pixels area centered around the maximum. Positions were estimated using either Gaussian fitting or center of mass calculation. Drift was corrected using a direct cross-correlation algorithm using the sample itself as a reference (no fiducial markers were used).
Event-based data were processed as follows. Positive events were binned in Δt=20 ms frames, on which PSFs were detected using a wavelet algorithm. This yielded the rough reference space and time positions x_0, y_0 and T_0 for each PSF. Molecules were then localized from a subset of all the events (both positive and negative) corresponding to an area of ± 4 pixels around (x_0,y_0) and to times in the interval $[T_0 - 60 \text{ ms}, T_0 + 120 \text{ ms}]$. The position of the center was estimated using a center of mass calculation. Other data were extracted—the total number of events N in the subset, the time of the rising edge t_+ (taken as the mean time of the positive events) and the time of the falling edge t_- (taken as the mean time of the negative events). These were used to calculate the ON time of each molecule $t_{ON} = t_- - t_+$. Positions were drift corrected using the same direct cross-correlation as for the frame-based data.

High density biological experiments (Fig. 4b–d). EMCCD acquisitions were done with a 30 ms exposure time and a gain of 100, and event-based were done with thresholds corresponding to the level of sensitivity called 'high' in the characterization. The detection path used either a 50:50 non-polarizing beamsplitter cube or a mirror to send all the photons on the event-based sensor. Both sensors were not synchronized but dual-view acquisitions were started and stopped simultaneously. We used a dSTORM buffer composed of 100 mg/ml glucose, 3.86 mg/ml MEA, 0.5 mg/ml glucose oxidase and 1.18 µl/ml catalase in PBS and a 638 nm continuous excitation with an irradiance of 5 kW/cm^2. No pumping phase was allowed, so the acquisitions were started immediately and stopped after 250 seconds. A low power continuous 405 nm excitation was also used during the entire acquisition to increase the detection density.
EMCCD frames were processed using a wavelet algorithm to detect the PSFs and each PSF was localized on a ± 3 pixels area centered around the maximum. Positions were estimated using either Gaussian fitting or center of mass calculation. Drift was corrected using a direct cross-correlation algorithm using the sample itself as a reference (no fiducial markers were used).

bioRxiv preprint doi: https://doi.org/10.1101/2022.07.22.501162; this version posted July 24, 2022. The copyright holder for this preprint (which was not certified by peer review) is the author/funder, who has granted bioRxiv a license to display the preprint in perpetuity. It is made available under aCC-BY-ND 4.0 International license.

Event-based data were processed as follows. The dataset was split in two subsets containing the positive and negative events respectively. Positive events were binned in Δt=10 ms frames, on which PSFs were detected using a wavelet algorithm. This yielded the rough reference space and time positions x_0, y_0 and T_0 for each PSF. Molecules were then localized from a subset of all the events (both positive and negative) corresponding to an area of ± 3 pixels around (x_0,y_0) and to times in the interval $[T_0 - 30 \text{ ms}, T_0 + 30 \text{ ms}]$. The position of the center was estimated using a center of mass calculation. The total number of events N in the subset corresponding to the molecule was also extracted. The same processing was run on the negative events subset with the same parameters. Due to the separate processing of the positive and negative events, the ON times could not be extracted since we did not use a dedicated program to link the rising and falling edges. Positions were drift corrected using the same direct cross-correlation as for the frame-based data.

FRC resolution calculation All FRC resolution measurements were done using the Fiji plugin NanoJ-SQUIRREL [37]. Localization lists were randomly split in two statistically independent sets and super-resolution images were generated with a pixel size of 5 nm. FRC maps were calculated with a number of blocks per axis of 30 (for full images) or 10 (for zooms on small sub-regions). We noticed little variation of the results with the calculation parameters.

Cramér-Rao Lower Bound calculation (Fig. 2b). CRLB values were estimated for the EMCCD camera using equation 4 from [56]. The values of the parameters were measured experimentally.

Localization and data treatment software. The localization and data treatment software is described in the **Localization precision and response linearity measurement**, **Standard density biological experiments** and **High density biological experiments** Methods sections. It should be noted that no filtering was used in the event-based processing.
All the processing and rendering was performed using a home-written Python code. The function used to read the event files was borrowed from the Metavision SDK open samples.

Code availability. Processing codes are made available on Github at the following address:
`https://github.com/Clement-Cabriel/Evb-SMLM.git`
The repository contains the codes for reading files and converting them into frame stacks, and the single-molecule localization code will be added soon. More codes will be added in the future. Datasets are available on the same repository to test the codes.

Data availability. More datasets are available from the corresponding authors upon reasonable request.

References

[1] E. Betzig, G. H. Patterson, R. Sougrat, O. W. Lindwasser, S. Olenych, J. S. Bonifacino, M. W. Davidson, J. Lippincott-Schwartz, and H. F. Hess, "Imaging intracellular fluorescent proteins at nanometer resolution.," *Science (New York, N.Y.)*, vol. 313, pp. 1642–5, sep 2006.

[2] S. T. Hess, T. P. K. Girirajan, and M. D. Mason, "Ultra-high resolution imaging by fluorescence photoactivation localization microscopy.," *Biophysical journal*, vol. 91, pp. 4258–72, dec 2006.

[3] M. J. Rust, M. Bates, and X. Zhuang, "Sub-diffraction-limit imaging by stochastic optical reconstruction microscopy (STORM)," *Nature Methods*, vol. 3, pp. 793–796, aug 2006.

[4] F. Balzarotti, Y. Eilers, K. C. Gwosch, A. H. Gynnå, V. Westphal, F. D. Stefani, J. Elf, and S. W. Hell, "Nanometer resolution imaging and tracking of fluorescent molecules with minimal photon fluxes," *Science*, vol. 355, pp. 606–612, dec 2016.

[5] P. Jouchet, C. Cabriel, N. Bourg, M. Bardou, C. Poüs, E. Fort, and S. Lévêque-Fort, "Nanometric axial localization of single fluorescent molecules with modulated excitation," *Nature Photonics*, vol. 15, pp. 297–304, jan 2021.

bioRxiv preprint doi: https://doi.org/10.1101/2022.07.22.501162; this version posted July 24, 2022. The copyright holder for this preprint (which was not certified by peer review) is the author/funder, who has granted bioRxiv a license to display the preprint in perpetuity. It is made available under aCC-BY-ND 4.0 International license.

[6] G. V. Los, L. P. Encell, M. G. McDougall, D. D. Hartzell, N. Karassina, C. Zimprich, M. G. Wood, R. Learish, R. F. Ohana, M. Urh, D. Simpson, J. Mendez, K. Zimmerman, P. Otto, G. Vidugiris, J. Zhu, A. Darzins, D. H. Klaubert, R. F. Bulleit, and K. V. Wood, "HaloTag: A novel protein labeling technology for cell imaging and protein analysis," *ACS Chemical Biology*, vol. 3, no. 6, pp. 373–382, 2008.

[7] P. J. Bosch, I. R. Corrêa, M. H. Sonntag, J. Ibach, L. Brunsveld, J. S. Kanger, and V. Subramaniam, "Evaluation of fluorophores to label SNAP-tag fused proteins for multicolor single-molecule tracking microscopy in live cells.," *Biophysical journal*, vol. 107, pp. 803–14, aug 2014.

[8] M. Mikhaylova, B. M. C. Cloin, K. Finan, R. van den Berg, J. Teeuw, M. M. Kijanka, M. Sokolowski, E. a. Katrukha, M. Maidorn, F. Opazo, S. Moutel, M. Vantard, F. Perez, P. M. P. van Bergen en Henegouwen, C. C. Hoogenraad, H. Ewers, and L. C. Kapitein, "Resolving bundled microtubules using anti-tubulin nanobodies," *Nature Communications*, vol. 6, no. May, p. 7933, 2015.

[9] L. D. Lavis, "Teaching old dyes new tricks: Biological probes built from fluoresceins and rhodamines," *Annual Review of Biochemistry*, vol. 86, pp. 825–843, jun 2017.

[10] J. B. Grimm, T. A. Brown, B. P. English, T. Lionnet, and L. D. Lavis, "Synthesis of janelia fluor HaloTag and SNAP-tag ligands and their use in cellular imaging experiments," in *Methods in Molecular Biology*, pp. 179–188, Springer New York, 2017.

[11] I. Izeddin, J. Boulanger, V. Racine, C. Specht, A. Kechkar, D. Nair, A. Triller, D. Choquet, M. Dahan, and J. Sibarita, "Wavelet analysis for single molecule localization microscopy," *Optics Express*, vol. 20, p. 2081, jan 2012.

[12] M. Reisser, J. Hettich, T. Kuhn, A. P. Popp, A. Große-Berkenbusch, and J. C. M. Gebhardt, "Inferring quantity and qualities of superimposed reaction rates from single molecule survival time distributions," *Scientific Reports*, vol. 10, feb 2020.

[13] A. Heckert, L. Dahal, R. Tjian, and X. Darzacq, "Recovering mixtures of fast diffusing states from short single particle trajectories," *Biorxiv*, may 2021.

[14] M. Lelek, M. T. Gyparaki, G. Beliu, F. Schueder, J. Griffié, S. Manley, R. Jungmann, M. Sauer, M. Lakadamyali, and C. Zimmer, "Single-molecule localization microscopy," *Nature Reviews Methods Primers*, vol. 1, jun 2021.

[15] Y.-L. Wu, A. Tschanz, L. Krupnik, and J. Ries, "Quantitative data analysis in single-molecule localization microscopy," *Trends in Cell Biology*, vol. 30, pp. 837–851, nov 2020.

[16] B. Huang, W. Wang, M. Bates, and X. Zhuang, "Three-Dimensional Super-Resolution Imaging by Stochastic Optical Reconstruction Microscopy," *Science*, vol. 319, no. 5864, pp. 810–813, 2008.

[17] S. R. P. Pavani, M. A. Thompson, J. S. Biteen, S. J. Lord, N. Liu, R. J. Twieg, R. Piestun, and W. E. Moerner, "Three-dimensional, single-molecule fluorescence imaging beyond the diffraction limit by using a double-helix point spread function," *Proceedings of the National Academy of Sciences*, vol. 106, pp. 2995–2999, feb 2009.

[18] N. Bourg, C. Mayet, G. Dupuis, T. Barroca, P. Bon, S. Lécart, E. Fort, and S. Lévêque-Fort, "Direct optical nanoscopy with axially localized detection," *Nature Photonics*, no. August, 2015.

[19] C. Cabriel, N. Bourg, P. Jouchet, G. Dupuis, C. Leterrier, A. Baron, M.-A. Badet-Denisot, B. Vauzeilles, E. Fort, and S. Lévêque-Fort, "Combining 3d single molecule localization strategies for reproducible bioimaging," *Nature Communications*, vol. 10, apr 2019.

[20] S. A. Maynard, P. Rostaing, N. Schaefer, O. Gemin, A. Candat, A. Dumoulin, C. Villmann, A. Triller, and C. G. Specht, "Identification of a stereotypic molecular arrangement of endogenous glycine receptors at spinal cord synapses," *eLife*, vol. 10, dec 2021.

bioRxiv preprint doi: https://doi.org/10.1101/2022.07.22.501162; this version posted July 24, 2022. The copyright holder for this preprint (which was not certified by peer review) is the author/funder, who has granted bioRxiv a license to display the preprint in perpetuity. It is made available under aCC-BY-ND 4.0 International license.

[21] I. M. Khater, I. R. Nabi, and G. Hamarneh, "A review of super-resolution single-molecule localization microscopy cluster analysis and quantification methods," *Patterns*, vol. 1, p. 100038, jun 2020.

[22] H. Verdier, F. Laurent, A. Cassé, C. L. Vestergaard, C. G. Specht, and J.-B. Masson, "A maximum mean discrepancy approach reveals subtle changes in α-synuclein dynamics," *bioRxiv*, apr 2022.

[23] A. Lampe, V. Haucke, S. J. Sigrist, M. Heilemann, and J. Schmoranzer, "Multi-colour direct STORM with red emitting carbocyanines," *Biology of the Cell*, vol. 104, no. 4, pp. 229–237, 2012.

[24] Z. Zhang, S. J. Kenny, M. Hauser, W. Li, and K. Xu, "Ultrahigh-throughput single-molecule spectroscopy and spectrally resolved super-resolution microscopy," *Nature Methods*, no. august, 2015.

[25] C. A. Valades Cruz, H. A. Shaban, A. Kress, N. Bertaux, S. Monneret, M. Mavrakis, J. Savatier, and S. Brasselet, "Quantitative nanoscale imaging of orientational order in biological filaments by polarized superresolution microscopy," *Proceedings of the National Academy of Sciences*, p. 201516811, 2016.

[26] A. Kinkhabwala, Z. Yu, S. Fan, Y. Avlasevich, K. MÃ¼llen, and W. E. Moerner, "Large single-molecule fluorescence enhancements produced by a bowtie nanoantenna," *Nature Photonics*, vol. 3, pp. 654–657, oct 2009.

[27] E. Lerner, T. Cordes, A. Ingargiola, Y. Alhadid, S. Chung, X. Michalet, and S. Weiss, "Toward dynamic structural biology: Two decades of single-molecule fÃ¶rster resonance energy transfer," *Science*, vol. 359, jan 2018.

[28] D. Bouchet, J. Scholler, G. Blanquer, Y. D. Wilde, I. Izeddin, and V. Krachmalnicoff, "Probing near-field light–matter interactions with single-molecule lifetime imaging," *Optica*, vol. 6, p. 135, jan 2019.

[29] G. Blanquer, B. van Dam, A. Gulinatti, G. Acconcia, Y. D. Wilde, I. Izeddin, and V. Krachmalnicoff, "Relocating single molecules in super-resolved fluorescence lifetime images near a plasmonic nanostructure," *ACS Photonics*, vol. 7, pp. 393–400, jan 2020.

[30] A. F. Koenderink, R. Tsukanov, J. Enderlein, I. Izeddin, and V. Krachmalnicoff, "Super-resolution imaging: when biophysics meets nanophotonics," *Nanophotonics*, vol. 11, pp. 169–202, dec 2021.

[31] N. Oleksiievets, Y. Sargsyan, J. C. Thiele, N. Mougios, S. Sograte-Idrissi, O. Nevskyi, I. Gregor, F. Opazo, S. Thoms, J. Enderlein, and R. Tsukanov, "Fluorescence lifetime DNA-PAINT for multiplexed super-resolution imaging of cells," *Communications Biology*, vol. 5, jan 2022.

[32] A. Beghin, A. Kechkar, C. Butler, F. Levet, M. Cabillic, O. Rossier, G. Giannone, R. Galland, D. Choquet, and J.-B. Sibarita, "Localization-based super-resolution imaging meets high-content screening," *Nature Methods*, vol. 14, pp. 1184–1190, oct 2017.

[33] D. Mahecic, W. L. Stepp, C. Zhang, J. Griffié, M. Weigert, and S. Manley, "Event-driven acquisition for content-enriched microscopy," *bioRxiv*, 2022.

[34] F. Liao, F. Zhou, and Y. Chai, "Neuromorphic vision sensors: Principle, progress and perspectives," *Journal of Semiconductors*, vol. 42, p. 013105, jan 2021.

[35] "Prophesee gen4.1 product brief: https://support.prophesee.ai/portal/en/kb/articles/evk4-hd-product-brief."

[36] B. Nieuwenhuizen, Robert P. J.;Lidke, Keith; Bates, Mark; Stallinga, Sjoerd; Rieger, "Image Resolution in Optical Nanoscopy," *Nature Methods*, vol. 6, no. 10, pp. 1199–1216, 2013.

bioRxiv preprint doi: https://doi.org/10.1101/2022.07.22.501162; this version posted July 24, 2022. The copyright holder for this preprint (which was not certified by peer review) is the author/funder, who has granted bioRxiv a license to display the preprint in perpetuity. It is made available under aCC-BY-ND 4.0 International license.

[37] S. Culley, D. Albrecht, C. Jacobs, P. M. Pereira, C. Leterrier, J. Mercer, and R. Henriques, "Quantitative mapping and minimization of super-resolution optical imaging artifacts," *Nature Methods*, vol. 15, pp. 263–266, feb 2018.

[38] O. K. Wade, J. B. Woehrstein, P. C. Nickels, S. Strauss, F. Stehr, J. Stein, F. Schueder, M. T. Strauss, M. Ganji, J. Schnitzbauer, H. Grabmayr, P. Yin, P. Schwille, and R. Jungmann, "124-color super-resolution imaging by engineering DNA-PAINT blinking kinetics," *Nano Letters*, vol. 19, pp. 2641–2646, mar 2019.

[39] J. E. Donehue, E. Wertz, C. N. Talicska, and J. S. Biteen, "Plasmon-enhanced brightness and photostability from single fluorescent proteins coupled to gold nanorods," *The Journal of Physical Chemistry C*, vol. 118, pp. 15027–15035, jun 2014.

[40] T. Dertinger, R. Colyer, G. Iyer, S. Weiss, and J. Enderlein, "Fast, background-free, 3d super-resolution optical fluctuation imaging (SOFI)," *Proceedings of the National Academy of Sciences*, vol. 106, pp. 22287–22292, dec 2009.

[41] S. Geissbuehler, C. Dellagiacoma, and T. Lasser, "Comparison between SOFI and STORM," *Biomedical Optics Express*, vol. 2, p. 408, jan 2011.

[42] S. Hugelier, J. J. de Rooi, R. Bernex, S. Duwé, O. Devos, M. Sliwa, P. Dedecker, P. H. C. Eilers, and C. Ruckebusch, "Sparse deconvolution of high-density super-resolution images," *Scientific Reports*, vol. 6, feb 2016.

[43] A. Speiser, L.-R. MÃ¼ller, P. Hoess, U. Matti, C. J. Obara, W. R. Legant, A. Kreshuk, J. H. Macke, J. Ries, and S. C. Turaga, "Deep learning enables fast and dense single-molecule localization with high accuracy," *Nature Methods*, vol. 18, pp. 1082–1090, sep 2021.

[44] A. Aristov, B. Lelandais, E. Rensen, and C. Zimmer, "ZOLA-3d allows flexible 3d localization microscopy over an adjustable axial range," *Nature Communications*, vol. 9, jun 2018.

[45] E. R. Weeks, "Introduction to the colloidal glass transition," *ACS Macro Letters*, vol. 6, pp. 27–34, dec 2016.

[46] C. R. Nugent, K. V. Edmond, H. N. Patel, and E. R. Weeks, "Colloidal glass transition observed in confinement," *Physical Review Letters*, vol. 99, p. 025702, jul 2007.

[47] S. W. Hell, "Far-field optical nanoscopy," *Science*, vol. 316, pp. 1153–1158, may 2007.

[48] H. P. Babcock and X. Zhuang, "Analyzing single molecule localization microscopy data using cubic splines," *Scientific Reports*, vol. 7, apr 2017.

[49] E. Nehme, D. Freedman, R. Gordon, B. Ferdman, L. E. Weiss, O. Alalouf, T. Naor, R. Orange, T. Michaeli, and Y. Shechtman, "DeepSTORM3d: dense 3d localization microscopy and PSF design by deep learning," *Nature Methods*, vol. 17, pp. 734–740, jun 2020.

[50] N. Boyd, E. Jonas, H. Babcock, and B. Recht, "Deeploco: Fast 3d localization microscopy using neural networks," *bioRxiv*, 2018.

[51] P. A. Gómez-García, E. T. Garbacik, J. J. Otterstrom, M. F. Garcia-Parajo, and M. Lakadamyali, "Excitation-multiplexed multicolor superresolution imaging with fm-STORM and fm-DNA-PAINT," *Proceedings of the National Academy of Sciences*, vol. 115, pp. 12991–12996, dec 2018.

[52] L. Gu, Y. Li, S. Zhang, Y. Xue, W. Li, D. Li, T. Xu, and W. Ji, "Molecular resolution imaging by repetitive optical selective exposure," *Nature Methods*, vol. 16, pp. 1114–1118, sep 2019.

[53] J. Cnossen, T. Hinsdale, R. Ø. Thorsen, M. Siemons, F. Schueder, R. Jungmann, C. S. Smith, B. Rieger, and S. Stallinga, "Localization microscopy at doubled precision with patterned illumination," *Nature Methods*, vol. 17, pp. 59–63, dec 2019.

bioRxiv preprint doi: https://doi.org/10.1101/2022.07.22.501162; this version posted July 24, 2022. The copyright holder for this preprint (which was not certified by peer review) is the author/funder, who has granted bioRxiv a license to display the preprint in perpetuity. It is made available under aCC-BY-ND 4.0 International license.

[54] L. Gu, Y. Li, S. Zhang, M. Zhou, Y. Xue, W. Li, T. Xu, and W. Ji, "Molecular-scale axial localization by repetitive optical selective exposure," *Nature Methods*, vol. 18, pp. 369–373, apr 2021.

[55] R. Ø. Thorsen, C. N. Hulleman, B. Rieger, and S. Stallinga, "Photon efficient orientation estimation using polarization modulation in single-molecule localization microscopy," *Biomedical Optics Express*, vol. 13, p. 2835, apr 2022.

[56] S. Stallinga and B. Rieger, "The effect of background on localization uncertainty in single emitter imaging," in *2012 9th IEEE International Symposium on Biomedical Imaging (ISBI)*, pp. 988–991, IEEE, may 2012.

bioRxiv preprint doi: https://doi.org/10.1101/2022.07.22.501162; this version posted July 24, 2022. The copyright holder for this preprint (which was not certified by peer review) is the author/funder, who has granted bioRxiv a license to display the preprint in perpetuity. It is made available under aCC-BY-ND 4.0 International license.

Supplementary material

Single molecule localization microscopy using event-based vision sensors allows imaging of dense molecules

Clément Cabriel*, Christian G. Specht and Ignacio Izeddin**

*Corresponding author: clement.cabriel@espci.fr, cabriel.clement@gmail.com
**Corresponding author: ignacio.izeddin@espci.fr

July 22, 2022

Supplementary Figure 1: FRC resolution measurements on the acquisitions presented in **Fig. 3**.

Supplementary Figure 2: Frames extracted from the acquisition presented in **Fig. 4**.

Supplementary Table 1: FRC resolution measurements on all the biological samples presented.

bioRxiv preprint doi: https://doi.org/10.1101/2022.07.22.501162; this version posted July 24, 2022. The copyright holder for this preprint (which was not certified by peer review) is the author/funder, who has granted bioRxiv a license to display the preprint in perpetuity. It is made available under aCC-BY-ND 4.0 International license.

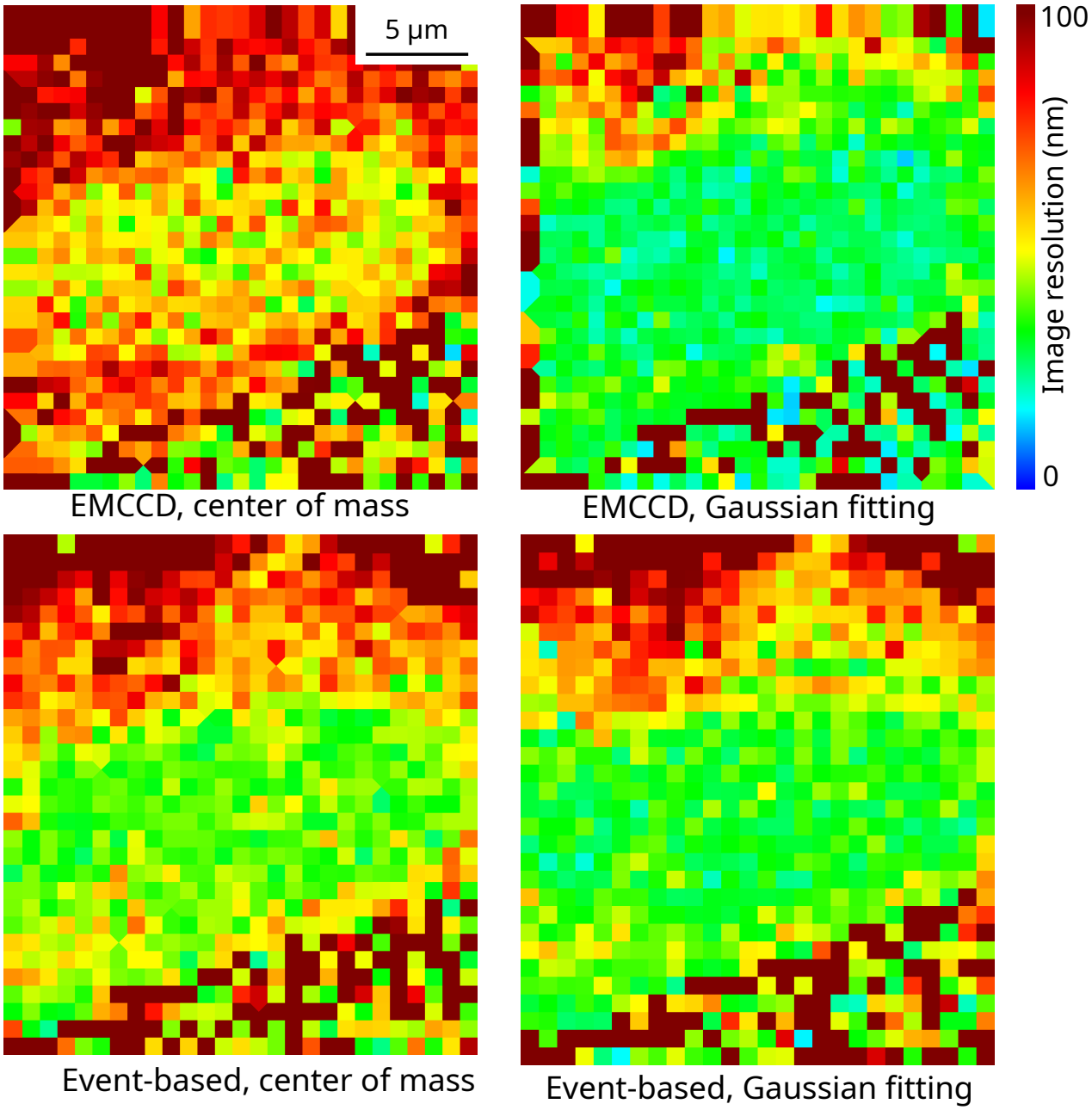

Supplementary Figure 1: FRC resolution measurements on fixed COS-7 cells labelled with AF647 against α-tubulin obtained with the event-based sensor and the EMCCD camera using a 50:50 beam-splitter in the detection path (corresponding to the data displayed in **Fig. 3**).

bioRxiv preprint doi: https://doi.org/10.1101/2022.07.22.501162; this version posted July 24, 2022. The copyright holder for this preprint (which was not certified by peer review) is the author/funder, who has granted bioRxiv a license to display the preprint in perpetuity. It is made available under aCC-BY-ND 4.0 International license.

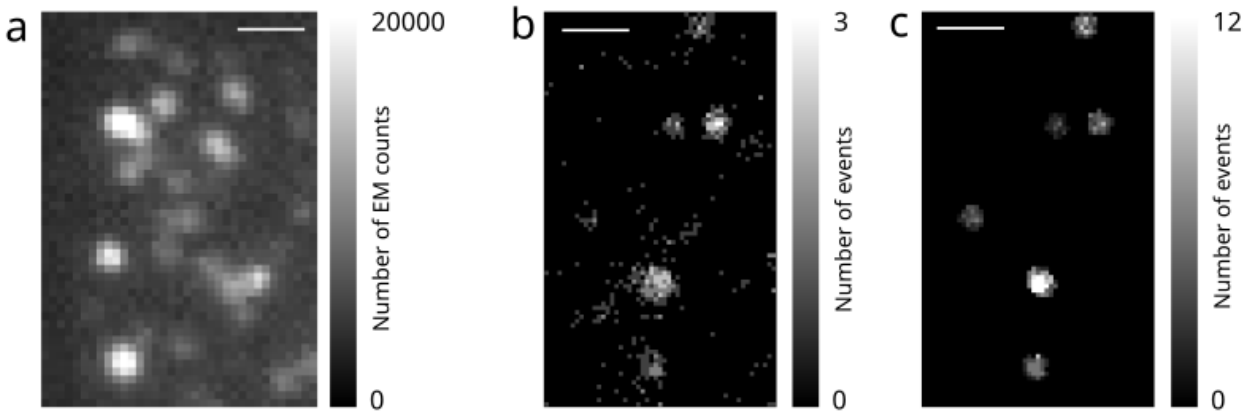

Supplementary Figure 2: Frames extracted from an acquisition on fixed COS-7 cells labelled with AF647 against α-tubulin acquired with a 50:50 beamsplitter over 250 seconds in a dense regime where the PSF exhibit noticeable overlap (presented in **Fig. 4**). **a** Single 30 ms exposure frame taken from the EMCCD. **b** Single frame (corresponding to a slightly different instant in the acquisition as **a**) generated from all the positive events detected in $\Delta t = 10$ ms (this frame is used only for the PSF detection). **c** Frame generated from all the positive events used for the localization of the PSFs detected in the $\Delta t = 10$ ms frame, i.e. in a time window of $[-30\text{ ms}, 30\text{ ms}]$ around the mean time of each molecule. Note the difference of event number compared to **b**. Scale bars: 1 µm.

bioRxiv preprint doi: https://doi.org/10.1101/2022.07.22.501162; this version posted July 24, 2022. The copyright holder for this preprint (which was not certified by peer review) is the author/funder, who has granted bioRxiv a license to display the preprint in perpetuity. It is made available under aCC-BY-ND 4.0 International license.

Acquisition conditions	Corresponding figure	Sensor and localization method	Average resolution (nm)
Standard density, full field, 50:50 beamsplitter	**Fig. 3a**	Event-based, center of mass Event-based, Gaussian fitting EMCCD, center of mass EMCCD, Gaussian fitting	36 30 50 28
Standard density, zoom, 50:50 beamsplitter	**Fig. 3b**	Event-based, center of mass Event-based, Gaussian fitting EMCCD, center of mass EMCCD, Gaussian fitting	34 28 27 44
Standard density, full field, 100 % on the event-based sensor	**Fig. 3d** left	Event-based, center of mass Event-based, Gaussian fitting	28 24
Standard density, zoom, 100 % on the event-based sensor	**Fig. 3d** right	Event-based, center of mass Event-based, Gaussian fitting	28 23
High density, full field, 50:50 beamsplitter	**Fig. 4d**	Event-based, center of mass Event-based, Gaussian fitting EMCCD, center of mass EMCCD, Gaussian fitting	64 64 136 92
Standard density, zoom, 50:50 beamsplitter	**Fig. 4c**	Event-based, center of mass Event-based, Gaussian fitting EMCCD, center of mass EMCCD, Gaussian fitting	57 55 114 84

Supplementary Table 1: FRC resolution measurements on fixed COS-7 cells labelled with AF647 against α-tubulin under various acquisition conditions.